nuclear fusion
IAEA

PAPER

Alfvén eigenmode properties and dynamics in the TJ-II stellarator

To cite this article: A.V. Melnikov *et al* 2012 *Nucl. Fusion* **52** 123004

View the article online for updates and enhancements.

You may also like

- ECRH effect on the electric potential and turbulence in the TJ-II stellarator and T-10 tokamak plasmas
A V Melnikov, L I Krupnik, E Ascasibar et al.
- Overview of the TJ-II stellarator research programme towards model validation in fusion plasmas
C. Hidalgo, E. Ascasíbar, D. Alegre et al.
- 2D distributions of potential and density mean-values and oscillations in the ECRH and NBI plasmas at the TJ-II stellarator
A V Melnikov, L G Eliseev, J M Barcala et al.

This content was downloaded from IP address 143.107.135.170 on 08/12/2022 at 21:57

Nucl. Fusion **52** (2012) 123004 (9pp) doi:10.1088/0029-5515/52/12/123004

Alfvén eigenmode properties and dynamics in the TJ-II stellarator

A.V. Melnikov[1], L.G. Eliseev[1], E. Ascasibar[2], A.A. Chmyga[3], C. Hidalgo[2], T. Ido[4], R. Jiménez-Gómez[2], A.D. Komarov[3], A.S. Kozachek[3], L.I. Krupnik[3], S.M. Khrebtov[3], A. Könies[5], Yu.K. Kuznetsov[6], A. López-Fraguas[2], S.E. Lysenko[1], V.A. Mavrin[1], K. Nagaoka[4], J.L. de Pablos[2], M.A. Pedrosa[2], S.V. Perfilov[1], A.I. Smolyakov[7], D.A. Spong[8], M.V. Ufimtsev[9], S. Yamamoto[10] and the TJ-II Team[2]

[1] Institute of Tokamak Physics, NRC 'Kurchatov Institute', 123182, Moscow, Russia
[2] Asociación EURATOM-CIEMAT, 28040, Madrid, Spain
[3] Institute of Plasma Physics, NSC KIPT, 61108, Kharkov, Ukraine
[4] National Institute for Fusion Science, 322-6 Oroshi-cho, Toki 509-5292, Japan
[5] Max-Planck-Institut für Plasmaphysik, EURATOM-Association, D-17491, Greifswald, Germany
[6] Institute of Physics, University of Sao Paulo, Sao Paulo, 05508-090, Brazil
[7] Department of Physics & Engineering Physics, University of Saskatchewan, 116 Science Place, Saskatoon SK S7N 5E2, Canada
[8] Oak Ridge National Laboratory, Oak Ridge, TN 37831-6169, USA
[9] Department of Computational Mathematics and Cybernetics, Moscow State University, Russia
[10] Institute of Advanced Energy, Kyoto University, Kyoto 611-0011, Japan

E-mail: melnik@nfi.kiae.ru

Received 4 April 2012, accepted for publication 8 October 2012
Published 2 November 2012
Online at stacks.iop.org/NF/52/123004

Abstract
Alfvén eigenmodes (AEs) were studied in neutral beam injection (NBI) heated plasmas in the TJ-II stellarator using a heavy ion beam probe (HIBP) in the core, and by Langmuir (LP) and Mirnov probes (MP) at the edge. AEs were detected over the whole plasma radius by the HIBP with a spatial resolution of about 1 cm. AE-induced oscillations were detected in the plasma density n_e, electric potential φ and poloidal magnetic field B_{pol} with frequencies $50\,\text{kHz} < f_{AE} < 300\,\text{kHz}$. The LP, MP and HIBP data showed a high level of coherency for specific branches of AEs. Poloidal mode wave-vectors k_θ, mode numbers m ($m < 8$) and propagation velocities $V_\theta \sim 30\,\text{km}\,\text{s}^{-1}$ were detected for various branches of AEs, having different radial locations. When the density rose due to NBI fuelling, the AE frequency decreased as predicted by the Alfvén law $f_{AE} \sim n_e^{-1/2}$. During the AE frequency decay the following new AE features were observed: (i) the poloidal wave-vector k_θ and mode number m remained constant, (ii) the cross-phases between the oscillations in B_{pol}, n_e and electric potential remained constant, having an individual value for each AE branch, (iii) V_θ decreased proportional to the AE frequency. The interaction of the AEs with the bulk (thermal) plasma resulted in clearly pronounced quasi-coherent peaks in the electrostatic turbulent particle flux spectra. Various AE branches exhibited different contributions to the particle flux: outward, inward and also zero, depending on the phase relations between the oscillations in E_{pol} and n_e, which are specific for each branch. A comparison with MHD mode modelling indicated that some of the more prominent frequency branches can be identified as radially extended helical AEs.

1. Introduction

It is widely recognized that energetic ion driven Alfvén eigenmodes (AEs) are an important element affecting the transport of fast particles in a future reactor. Mirnov probes (MP) are conventionally used to characterize the poloidal m and toroidal n mode numbers and spectral characteristics of AEs [1]. Heavy ion beam probing (HIBP), which is used

 © 2012 IAEA, Vienna Printed in the UK & the USA

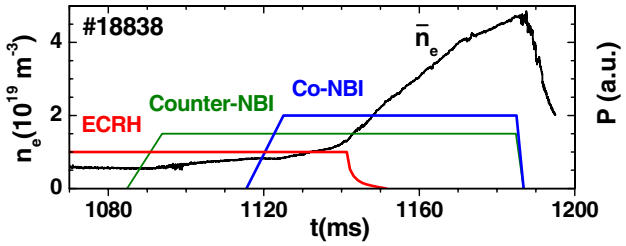

Figure 1. A typical discharge scenario in TJ-II. Standard magnetic configuration 100_44_64, $P_{\rm ECRH} = 0.6$ MW, off-axis, $\rho_{\rm ECRH} = 0.34$, and total $P_{\rm NBI} = 0.9$ MW, co- and counter-injection. Powers are not shown to scale.

for plasma potential profile measurements [2] and also for electrostatic plasma oscillations such as GAMs [3, 4], has been recently developed as a new tool to study AEs with high spatial and frequency resolution in the core plasma [5, 6].

Using HIBP we observed AEs in the TJ-II heliac with good spatial resolution (∼1 cm) over the whole plasma cross-section. This paper summarizes new observations of the phenomenology and features of the neutral beam injection (NBI)-induced AEs, and modelling efforts performed to identify the most pronounced AEs observed in TJ-II so far.

2. Experimental set-up

The main parameters of the low magnetic shear stellarator TJ-II with helical axis and bean-like plasma shape are given as follows: toroidal magnetic field $B_{\rm tor} = 1$ T, mean major radius $\langle R\rangle = 1.5$ m, mean minor radius $\langle a\rangle = 0.22$ m and line-averaged density $\bar{n}_{\rm e} = (0.3\text{–}6) \times 10^{19}\,{\rm m}^{-3}$. TJ-II is a flexible four-field-period heliac with magnetic configurations that can be changed by independent settings of the currents in the magnetic coils. The L-mode hydrogen plasmas described in this paper were obtained in a configuration referred to as 'standard' and labelled 100_44_64, where the numbers refer to the currents in the coils. Additional heating at TJ-II consists of two gyrotrons with a total power of up to $P_{\rm ECRH} = 0.3$ MW each, and two neutral beam injectors (NBI) that generate H^0 beams with energies up to 32 kV and total injected power of up to $P_{\rm NBI} = 0.45$ MW each. Various types of Alfvénic activities may be excited in such NBI-heated plasmas [1, 2, 5]. The 'co-' ('counter-') injector is directed along (against) the toroidal field of the device and the NBI-driven current increases (decreases) slightly the rotational transform with respect to the vacuum one.

A typical discharge scenario is presented in figure 1. The plasma was created and heated initially by off-axis ECRH. Later on it was auxiliary heated by counter-injection and then by co-injection. Due to the NBI fuelling, the plasma density starts to rise. At the initial stage, the density rise is not so strong, which is interpreted as a concurrency with ECRH-induced density pump-out. When the density exceeds the ECRH cut-off value $\bar{n}_{\rm cut\text{-}off} = 1.7 \times 10^{19}\,{\rm m}^{-3}$, the plasma is sustained purely by NBI. At this stage of the discharge, a steep increase in the plasma density is observed. It has been recently found that under certain conditions, such as wall lithium coating, a spontaneous L–H transition may occur [7].

The plasma density and electron temperature profiles, measured by Thomson scattering, are presented in figure 2.

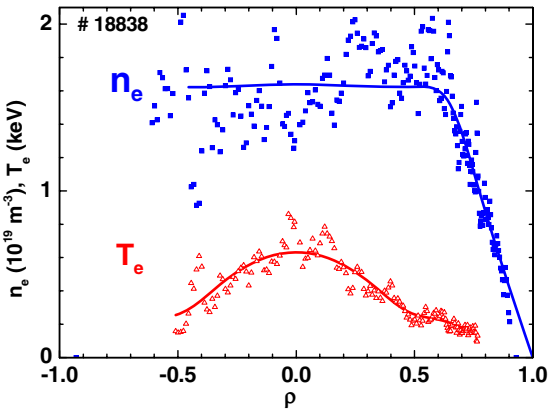

Figure 2. Typical density and temperature profiles, measured by Thomson scattering at $t = 1140$ in shot #18838. Solid lines are fitting curves.

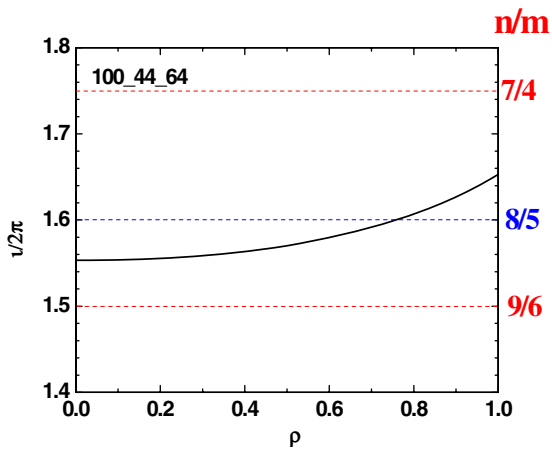

Figure 3. Profile of the rotational transform for the standard magnetic configuration. The low-order rational $\iota/2\pi = 8/5$ magnetic surface is located in the plasma area. Closely relevant resonances are also shown.

The plasma position is characterized by the radial coordinate ρ ($\sim x/a$ with the x coordinate along the outward horizontal axis) with $\rho > 0$ at the low-field side (LFS) and $\rho < 0$ at the high-field side (HFS) of the torus. Thomson scattering provides data at only one time point in the discharge. For the discharge discussed here profiles are obtained at $t = 1140$ ms, when all heating methods are active. The density profile is quite flat at the centre with a strong gradient at the periphery. The $T_{\rm e}$ profile has a parabolic shape. The radial profile of the rotational transform $\iota/2\pi = 1/q$ for the standard configuration is shown in figure 3.

For these parameters, the ratio of the beam ion velocity to the Alfvén velocity is $v_{\rm beam}/v_{\rm A} \sim 0.36$. There have been many observations on tokamaks that sub-Alfvénic velocities in this range can drive Alfvén instabilities and the theoretical basis for this was originally recognized [8] as being due to sideband coupling, i.e. since multiple modes are typically coupled for Alfvén instabilities, there will be a range of parallel wavenumbers present and fast ions can couple to the mode over a range of velocities, provided $v_{\rm beam} \sim f_{\rm AE}/k_\parallel$. For stellarators, mode coupling effects can be even more

significant, and Alfvén modes have been predicted to be unstable even for $v_{\rm beam}/v_{\rm A} \sim 0.1$ [9].

3. HIBP: a new diagnostic tool to study AEs

Recently, HIBP has become a new powerful tool to study AEs in TJ-II [1, 5]. HIBP in TJ-II operates with Cs^+ ions that have a probing beam energy $E_{\rm b} = 125\,{\rm keV}$ [10, 11]. HIBP provides the simultaneous measurement of three independent quantities: the plasma electric potential φ, density $n_{\rm e}$ and poloidal magnetic field $B_{\rm pol}$.

Currently, HIBP operates with two sample volumes, which are observed simultaneously. The two sample volumes are oriented in the poloidal direction to measure the poloidal component of the electric field $E_{\rm pol}$ by the difference in local potentials, $E_{\rm pol} = (\varphi_1 - \varphi_2)/x$, $x \sim 1\,{\rm cm}$, which limits the observed poloidal wave-vector, $k_\theta < 2\,{\rm cm}^{-1}$. These data provide the radial component of the drift velocity $V_{\boldsymbol{E}\times\boldsymbol{B}}$: $V_r = E_{\rm pol}/B_{\rm tor}$. Strong electromagnetic oscillations associated with AEs may create radial particle fluxes via several different mechanisms. Direct (and ambipolar) electrostatic particle flux is created by the oscillations of the poloidal electric field $\tilde{n}_{\rm e}\tilde{V}_r \sim \tilde{n}_{\rm e}(t)\tilde{E}_{\rm pol}$. The magnetic fluctuations may also contribute to the transport via $\tilde{j}_\parallel \tilde{B}_r/B$, with $\tilde{j}_\parallel$ representing the oscillations in the parallel plasma current. HIBP allows a direct determination of the radial electrostatic component of the turbulent particle flux in the core plasma $\Gamma_r(t) = \tilde{n}_{\rm e}\tilde{V}_r = 1/B_{\rm tor}\tilde{n}_{\rm e}(t)\tilde{E}_{\rm pol}(t) = \Gamma_{E\times B}$ in a similar way as Langmuir probes at the edge [12].

4. Mode observations using HIBP

The NBI-induced AEs are pronounced in the spectrogram of the power spectral density (PSD) of various plasma parameters such as plasma density, potential and $B_{\rm pol}$ as a single quasi-monochromatic peak or, more typically, a variety of such peaks, excited simultaneously. The set of low m ($m < 8$) branches, detected with high frequency resolution (up to 3 kHz) is expected to represent different types of AEs. A typical example of the temporal evolution of the AEs is presented in figures 4(*a*)–(*c*) for the same shot as in figure 1. Oscillations in the AE frequency range are observed in the PSD of the magnetic probe (figure 4(*a*)), HIBP beam current $I_{\rm t}$, representing the local density (figure 4(*b*)), HIBP plasma electric potential φ (figure 4(*c*)) and $B_{\rm pol}$, simultaneously detected by the HIBP and MP, as was described first in [5], in the frequency range $50\,{\rm kHz} < f_{\rm AE} < 330\,{\rm kHz}$. The frequencies of the various branches of AEs show a decay due to the density rise according to the Alfvénic frequency scaling $f_{\rm AE} \sim n_{\rm e}^{-1/2}$.

AEs are observed in both purely NBI-heated and in combined ECR- and NBI-heated plasmas; a high coherency between MP and HIBP data was found for specific branches of AEs.

5. AE cross-phase characteristics

HIBP is a multipurpose diagnostic tool, which provides simultaneous measurements of various plasma parameters for the same sample volume. The coherence and cross-phase between them may provide important characteristics of the AEs. Simultaneous poloidally resolved HIBP measurements provide the cross-phase of two separated signals, which is, in principle, sufficient to extract the poloidal wavelength, phase

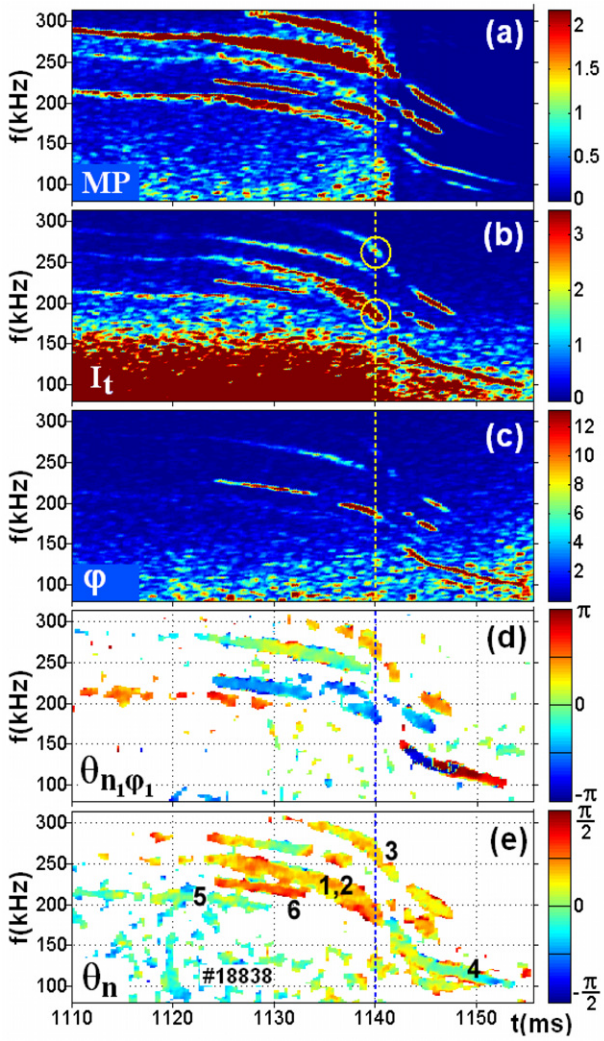

Figure 4. AEs observed in the PSD (*a*)–(*c*) and frequency-resolved cross-phase (*d*), (*e*) time evolution of HIBP ($\rho = -0.54$) and MP signals. (*a*) PSD of the MP signal; (*b*) PSD of the HIBP total secondary beam current $I_{\rm t}$ proportional to $n_{\rm e}$; (*c*) PSD of the HIBP plasma potential φ. The scales for the colour bars for PSDs are arbitrary and adapted to clearly highlight the various branches. (*d*) $\theta_{n1\,\varphi1}$—cross-phase between HIBP density and potential oscillations. Only points with ${\rm Coh}_{n1\,\varphi1} > 0.2$ are shown. (*e*) θ_n—cross-phase between HIBP densities, measured in two sample volumes. Only the points with ${\rm Coh}_{n1\,n2} > 0.3$ are shown. The colour bars for $\theta_{n1\,\varphi1}$ and θ_n are in radians. Yellow circles in (*b*) mark the modelled modes 1, 2 and 3, presented in figures 10, 11 and 12. Numbers in (*e*) show the modes, with calculated m's, presented in the table below:

Mode	θ/π	m
1, 2	0.182 ± 0.05	4.55 ± 1.25
3	0.148 ± 0.07	3.7 ± 1.75
4	0.024 ± 0.09	0.6 ± 2.25
5	-0.03 ± 0.07	-0.75 ± 1.75
6	0.26 ± 0.06	6.5 ± 1.5

velocity and mode number m. Following a similar approach as discussed in [13, 14], we estimate the coherency Coh_{xy} and cross-phase θ_{xy} between two signals $x(t)$ and $y(t)$, by the auto-power $S_{xx}(f,t)$ or PSD and cross-power $S_{xy}(f,t)$ Fourier spectrograms:

$$\mathrm{Coh}_{xy}(f,t) = |S_{xy}|/|S_{xx}S_{yy}|^{1/2},$$
$$q_{xy}(f,t) = \tan^{-1}\{\mathrm{Im}(S_{xy})/\mathrm{Re}(S_{xy})\}. \quad (1)$$

Figure 4(*d*) shows the cross-phase between plasma density and potential oscillations $\theta_{n1\varphi1}(f,t)$ as measured by the HIBP. When the density rises, the AE frequency f_{AE} decreases, consistent with $f_{\mathrm{AE}} \sim n_{\mathrm{e}}^{-1/2}$; however, $\theta_{n1\varphi1}$ remains nearly constant for each of the AE branches. This indicates that $\theta_{n1\varphi1}$ is associated with the individual characteristics of each AE branch.

For the poloidally propagating density perturbations we use the Fourier spectrogram $S_{n1n2}(f,t) = S^{I_t}_{1,2}(f,t)$ for two signals of the total beam current I_t, which provides $\theta_{n1n2} = \theta_n$, the cross-phase between the densities measured in two sample volumes [5]. The poloidal wave vector k_θ and mode number m are obtained from

$$k_\theta = \theta_n/\Delta x, \qquad m = Lk_\theta/2\pi, \quad (2)$$

where L is the circumference of the poloidal cross-section of the magnetic flux surface. Here we assume that k_θ is poloidally symmetric and the phase resolution is sufficient for the retrieval of the single mode. An example of the density phase spectrogram is presented in figure 4(*e*). In this figure a large number of AE branches with different values of m can be seen, excited simultaneously at the same radial location, $\rho = -0.54$, where $L = 83$ cm.

In the complicated magnetic geometry of TJ-II, k_θ is expected to be not exactly poloidally symmetric: in particular, k_θ should be smaller everywhere in the LFS and HFS than at the 'tips' of the bean. For example, for the AE corresponding to $\iota/2\pi = 8/5$ we numerically estimated the poloidal asymmetry in k_θ in the standard magnetic configuration and found for the HFS a correction factor of ~1.2 between the poloidally averaged k_θ and local measurements. This correction factor varies only slightly over the plasma radius. Therefore, the m values, presented in the table in the caption of figure 4, should be increased by approximately 20%.

Following the approach used in [1], it is also possible to obtain the parallel wave-vector $k_\parallel$ and the toroidal mode number n for each AE branch, using data for m and f_{AE} with the help of the relations

$$f_{\mathrm{AE}} = k_\parallel v_{\mathrm{A}}/2\pi, \qquad k_\parallel = |n - m\iota/2\pi|/R, \quad (3)$$

where $v_{\mathrm{A}} \sim B/\sqrt{n_{\mathrm{e}}}$ is the Alfvén velocity. For the data presented in figure 4, we find $k_\parallel$ values in the interval $0.16\,\mathrm{m}^{-1} < k_\parallel < 0.3\,\mathrm{m}^{-1}$. Using the experimentally deduced $k_\parallel$ values and assuming that the $\iota/2\pi$ profile is close to the vacuum one, it is possible to estimate the values for n applying the simplified expression (3) $n = m\iota/2\pi - Rk_\parallel$. We assumed $\iota/2\pi(0.54) = 1.57$ for the standard 100_44_64 configuration. Bearing in mind the correction factor 1.2 for m, we obtain $m = 5.5 \pm 1.5$ for modes 1 and 2, and thus estimate $n = 8.3 \pm 2.5$, and similarly $m = 4.4 \pm 2.2$ and $n = 6.6 \pm 3.2$ for mode 3.

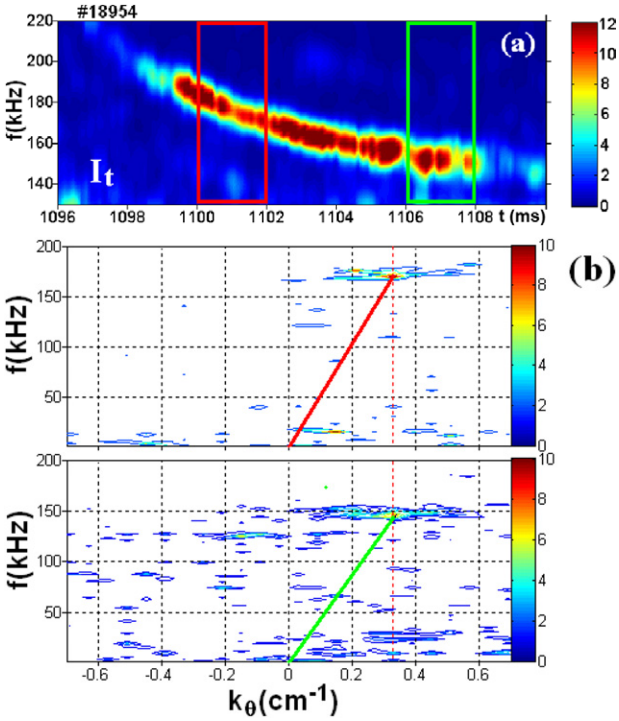

Figure 5. AE poloidal rotation at $\rho = -0.54$. (*a*) PSD of HIBP density spectrogram, (*b*) frequency–wave-vector spectrum$S(k_\theta, f)$ of HIBP density for two time intervals marked by red and green in (*a*). Colour bars are in arbitrary units to highlight the most prominent features in the spectra clearly.

6. Poloidal rotation dynamics associated with AEs

Poloidally resolved density and electric potential measurements provide the 2D frequency–poloidal wave-vector spectrum $S(k_\theta, f)$ [15]. An example of the density PSD obtained with 2 ms time resolution is shown in figure 5(*a*). The time evolution of the mode frequency is caused by the plasma density rise due to NBI fuelling. The spectra $S(k_\theta, f)$ for the marked time window are shown in figure 5(*b*). It clearly shows the mode pronounced above the background turbulence. In both time windows the k_θ value is the same, while the mode frequency is lower for higher density. The linear phase velocity of the AE poloidal rotation or poloidal propagation velocity is given by

$$V_\theta = 2\pi\, f/k_\theta. \quad (4)$$

In the upper box of figure 5(*b*), from $S(k_\theta, f)$ we find $V_\theta = 2\pi 170 \times 10^3/0.33(\mathrm{Hz\,cm}) = 32\,\mathrm{km\,s^{-1}}$, while for the lower box we find $f = 147$ kHz, $V_\theta = 28\,\mathrm{km\,s^{-1}}$. This figure also shows that the AE maintains its poloidal structure (m value) for a characteristic 'lifetime' of several milliseconds. The poloidal propagation velocity for the mode V_θ evolves due to the frequency evolution.

Fine details of the dynamics of the mode rotation can be analysed using a higher temporal resolution of the cross-phase spectrogram (512 points at 1 μs sampling). Figure 6 (left, upper box) shows the density cross-phase spectrogram for the mode branch presented in figure 5(*a*). The histograms of the cross-phase values, determined for the marked time interval, are shown in figure 6 (right). The density coherence and cross-phase show that a single mode exists over the whole analysed

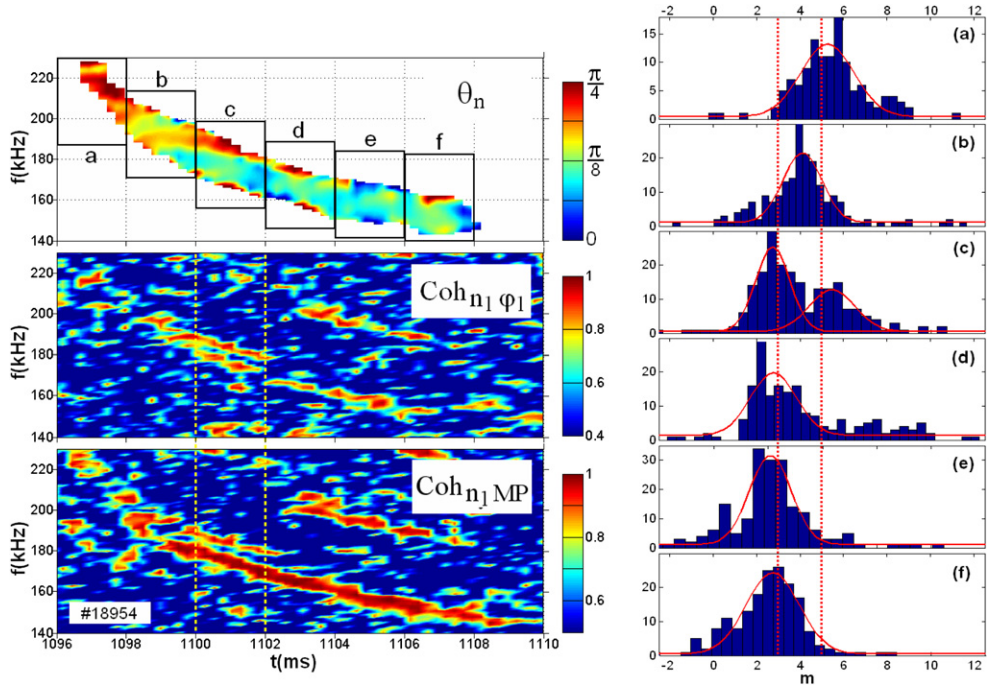

Figure 6. An example of the poloidal mode number determination. Left box: (i) upper figure: HIBP density cross-phase spectrogram θ_n. Only the points with high $\mathrm{Coh}_{n1n2} > 0.3$ are shown. The colour bar is in radians; (ii) middle figure: coherency between HIBP density and potential φ; (iii) bottom figure: coherency between HIBP density and MP signal. Right box: histograms of θ_n presented in terms of m, using formula (2), in the corresponding time windows. Time window 'c' ($t = 1100$–1102 ms) shows an example of the coexistence of two modes with close poloidal mode numbers $m = 3$ and $m = 5$, which are visible as two peaks in the phase histograms and in the spectrograms of coherency between density and potential or density and MP signal.

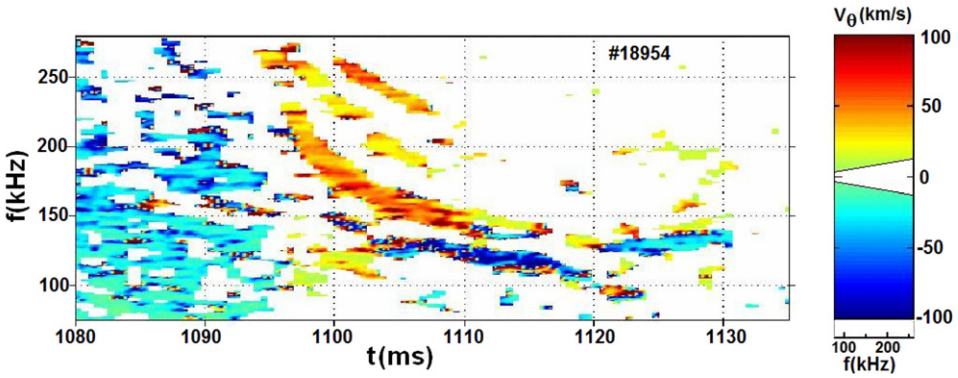

Figure 7. Poloidal phase velocity V_θ spectrogram for density perturbations at $\rho = -0.54$, shot #18954. Only the points with high $\mathrm{Coh}_{n1n2} > 0.3$ are shown. The colour bar represents the velocity. The white wedge denotes unresolved velocity interval caused by the finite $\Delta x = 1.66$ cm: $|V_\theta| \geqslant 2\pi f/|k_\theta^{\max}|$.

time window. There is, however, a temporal fine structure in this case detected by the coherency between HIBP density and potential $\mathrm{Coh}_{n1\varphi1}$ (left middle box) and coherency between HIBP density and MP signal $\mathrm{Coh}_{n1\,\mathrm{MP}}$ (left lower box). At the first two stages 'a' and 'b', the single mode really exists, the cross-phase gives $m = 5 \pm 1.25$. Then, at stage 'c' two peaks are visible, corresponding to $m = 5 \pm 1.5$ and $m = 2.75 \pm 1.5$, which implies the observation of two modes with close frequencies and different mode numbers: $m = 5$ and $m = 3$, existing simultaneously. Later on, at stages 'd', 'e' and 'f' the $m = 5$ mode vanishes and only the $m = 3$ mode remains. The mode propagation velocity $V_\theta = Lf/m$ evolves accordingly, decreasing continuously with decreasing frequency, $V_\theta \sim f_{\mathrm{AE}} \sim n_{\mathrm{e}}^{-1/2}$.

The example presented above shows that the coherency and phase resolution attainable in the experiment provide the poloidal mode number m in the case of a mode with a single dominant poloidal harmonic. In the case of multiple harmonics with comparable amplitude it might be more difficult to infer the spectrum of m values from the data. Case 'c' shows that at least two modes with comparable amplitudes may be resolved using the proposed phase histogram, which was obtained by cross-correlation with other signals. The other examples of mode evolution are presented in figure 4. The mode branches, presented there, show a constant mode number over a typical time interval of about 10 ms.

Figure 7 presents an example of the $V_\theta(f, t)$ spectrogram. The positive sign of k_θ and V_θ implies propagation in the electron diamagnetic drift direction. The figure shows that

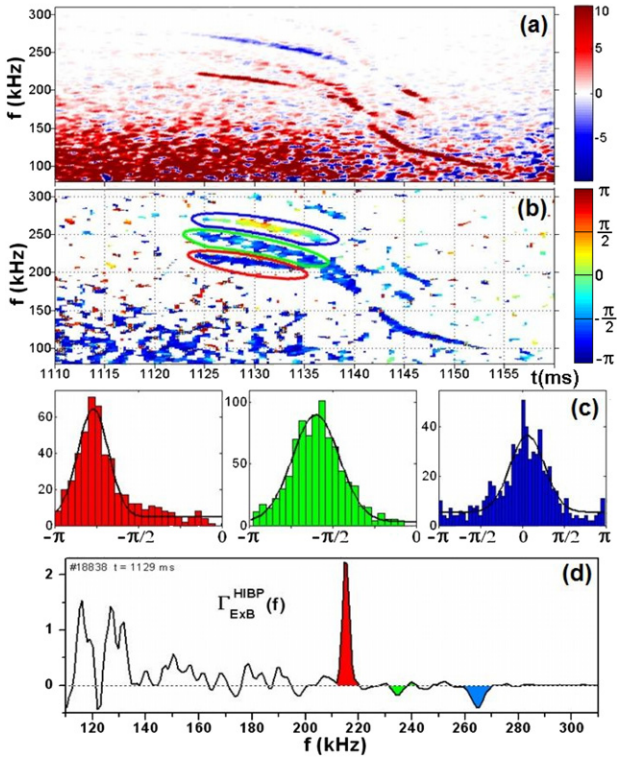

Figure 8. (*a*) Frequency-resolved turbulent particle flux (in arb. units) in the NBI-sustained discharge. Red colour means outward flux, and blue inward flux. The AEs are pronounced in the flux spectrogram, indicating that the AE contribution in the total turbulent flux is significant. (*b*) Cross-phase $\theta_{n_e E_{pol}}$ between n_e and E_{pol} oscillations. Only the points with high $\mathrm{Coh}_{n_e E_{pol}} > 0.3$ are shown. The colour bar is in radians. Three chosen branches of the AE are marked by colour ovals. (*c*) The histograms of the cross-phase for each marked branches with corresponding colours, indicating flux direction. Left box: $\theta_{n_e E_{pol}} = -3/4\pi$, corresponding to the outward flux, central box: $q_{n_e E_{pol}} = -\pi/2$, corresponding to zero flux, right box: $\theta_{n_e E_{pol}} \sim 0$, corresponding to the inward flux. (*d*) PSD of the turbulent particle flux, taken at some time instant,averaged over 1 ms. Three frequency peaks related to the branches of the AE identified above are marked with corresponding colours.

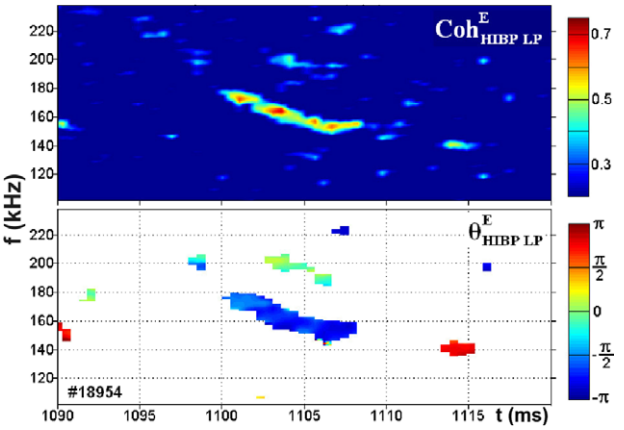

Figure 9. Time evolution of the coherency and cross-phase between E_{pol}, measured by HIBP in the core ($\rho = -0.54$), and E^{LP}_{pol}, measured by Langmuir probes (LP) in the edge ($\rho = -0.9$). Only the points with high $\mathrm{Coh}^{E}_{HIBP\ LP} > 0.3$ are shown in the phase spectrogram. The colour bar for the cross-phase is in radians.

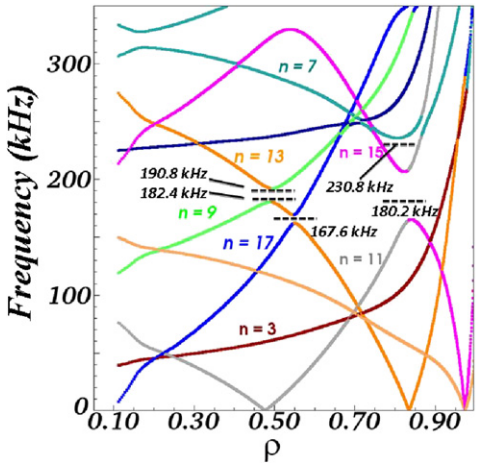

Figure 10. #18838: Alfvén continuum calculated by the STELLGAP code at $t = 1140$ ms. Alfvén mode frequencies and localizations indicated by black dashed lines.

various mode branches may rotate in the electron and ion diamagnetic drift directions.

7. Density perturbations and electrostatic particle flux induced by AE

The contribution of AEs to the transport of fast particles and thermal plasma particles is a key ingredient in the AE studies in fusion devices. The AE contribution to the bulk (thermal) plasma electrostatic turbulent particle flux was studied by HIBP, following the method described in [5]. Figure 8 presents the frequency-resolved turbulent particle flux in the NBI-sustained discharge. The flux related to broadband turbulence has an intermittent character [16]. It consists of a series of stochastic bursts, which are mostly directed outwards. On top of the broadband turbulence we see quite pronounced quasi-coherent peaks caused by AEs. Figure 8 shows that various AEs may have different features. Most of the modes contribute to the outward flux. On top of that, there are some modes, which produce the inward flux. Some of the AEs may produce no flux at all. The key ingredient for the flux direction (and value as well) is the phase relation between the density and E_{pol} oscillations. The cross-phase between n_e and E_{pol} oscillations $\theta_{n_e - E_{pol}}$ is different for these three cases, as shown in figure 8(*c*). It is important to note that pure Alfvén waves (in homogeneous plasmas) do not produce any density perturbations. In the inhomogeneous case, the density perturbations $\tilde{n}_e$ may be created either due to the gradient of plasma density (convective term) and/or due to plasma compressibility due to the inhomogeneous magnetic field (compressibility term) of the evolution equation for the density perturbation:

$$\frac{\partial \tilde{n}_e}{\partial t} = -\tilde{V}_{E\times B} \cdot \nabla n_0 + 2\tilde{V}_{E\times B} \cdot \nabla B/B, \qquad (5)$$

where n_0 is the equilibrium density and $\nabla B/B = \nabla \ln B$ is the gradient of the equilibrium magnetic field. This expression is valid for a low-pressure plasma. In the case under study, the plasma density is rather flat, see figure 1, and

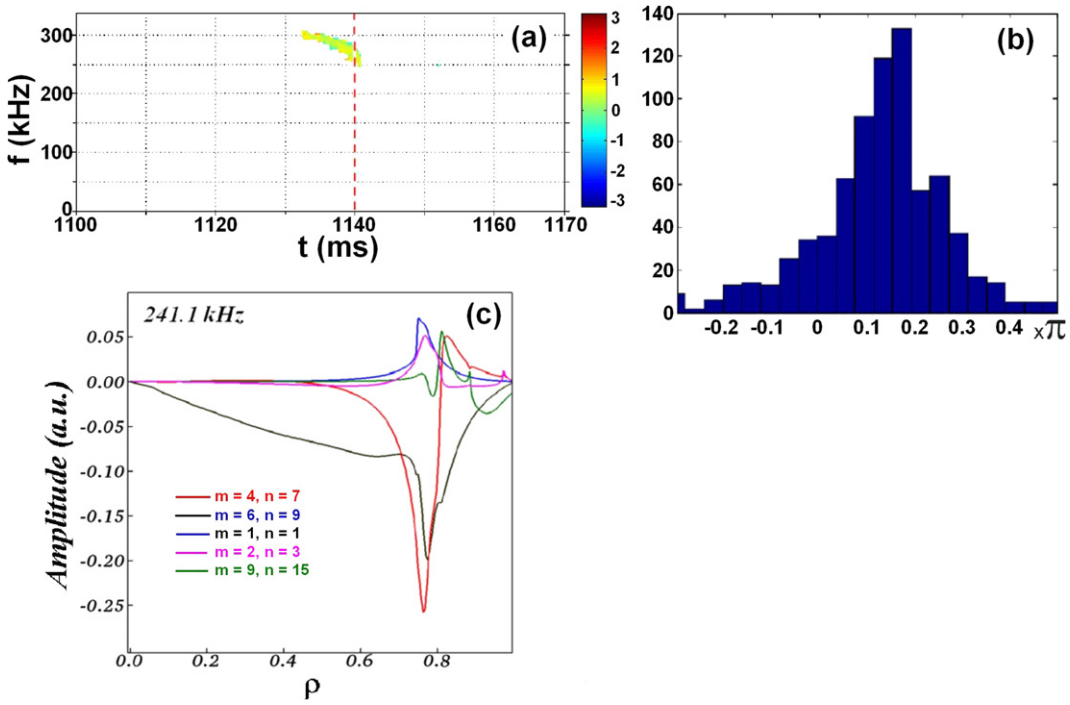

Figure 11. #18838: (*a*) spectrogram of cross-phase θ_n between n_e oscillations, observed in poloidally shifted sample volumes. Colour bar is in radians. The only branch under study is presented (3 from figure 4(*e*)); (*b*) the histogram of θ_n for the presented branch; $\theta/\pi = 0.148 \pm 0.07$, $m = 4.4 \pm 2.2$, $n = 6.6 \pm 3.2$; (*c*) the computed HAE structure of plasma potential at 241.1 kHz.

plasma compressibility should become a dominant mechanism for density perturbations. The importance of toroidal compressibility for density perturbations in Alfvén-type modes was noted in TFTR [17] and JET experiments [18]. In our experiment, the turbulent particle flux is determined directly from the measurements of full density perturbations and radial electric field, $\Gamma^{\mathrm{AE}}_{E\times B} = n_e V_r$, thus the density perturbation mechanism is not important. However, the nature of this mechanism is important in determining whether the net flux is diffusive or convective. It was noted earlier [19, 20] that the inhomogeneity of the phase space due to the gradient of the magnetic field leads to the appearance of pinch effects, rather than diffusive terms due to the inhomogeneity of plasma density.

It is worth mentioning that recently in low-density ECRH plasmas of TJ-II, another type of instability has been found, related to the supra-thermal electrons, which was also characterized by zero contribution to the turbulent particle flux [13]. Typically, the AE contribution to the frequency-resolved turbulent particle flux $\Gamma^{\mathrm{AE}}_{E\times B}$ was found to be a significant fraction of the total flux $\Gamma_{E\times B}$. Figure 8 shows that $\Gamma^{\mathrm{AE}}_{E\times B}$ exceeds the broadband turbulence flux $\Gamma^{\mathrm{BB}}_{E\times B}$ from the same frequency domain.

8. Radial extent of AEs

The existence of strong correlations between plasma potential, density and B_{pol}, as measured by HIBP, was reported in earlier papers [5, 20]. Strong correlations were also found between the core density measured by HIBP and MP signals. There is a remarkable feature of E_{pol}, induced by AEs. Some of the modes exhibit core–edge (long range) radial correlations

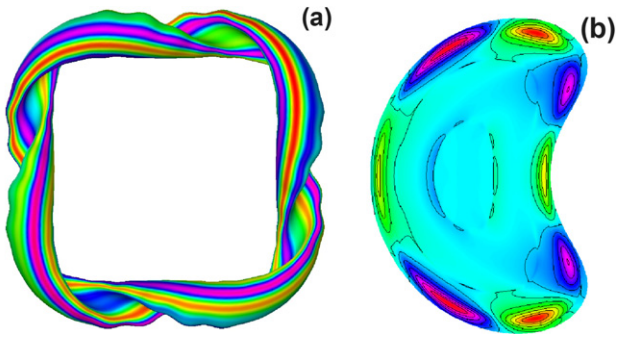

Figure 12. #18838: 3D mode structure of the identified HAE $n/m = 7/4$, (*a*) top view, (*b*) poloidal cut.

between E_{pol}, measured by HIBP in the core, and the poloidal electric field measured by Langmuir probes (LP) in the edge $E^{\mathrm{LP}}_{\mathrm{pol}} = (\varphi_1 - \varphi_2)^{\mathrm{float}}/x^{\mathrm{LP}}$, $x^{\mathrm{LP}} \sim 3$ mm. Figure 9 presents an example of such core–edge correlations. Note that the poloidal wave-vector measured with the LP is limited to $k^{\mathrm{LP}}_\theta < 10\,\mathrm{cm}^{-1}$, while $k^{\mathrm{HIBP}}_\theta < 2\,\mathrm{cm}^{-1}$.

The fact that a correlation is seen between the core and the edge by the two diagnostics despite their difference in the maximum accessible value for k_θ indicates that a longer poloidal wavelength (lower k_θ) component is responsible for this correlation. In the case presented in figure 9, the responsible wavelength is $k_\theta = 0.33\,\mathrm{cm}^{-1}$, as found for the density perturbation and shown in figure 5(*b*). Therefore, the considered AE is characterized by a large radial correlation length in the outer half of the plasma radius.

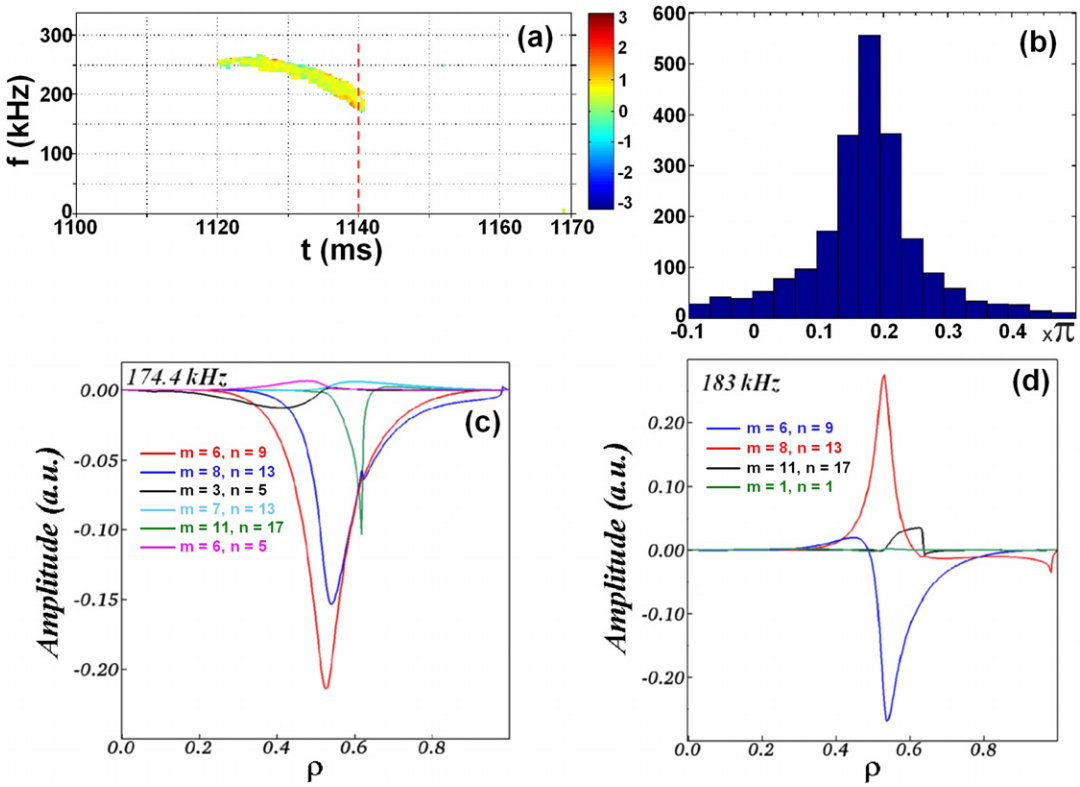

Figure 13. #18838: (*a*) Spectrogram of cross-phase θ_n for the branch under study (1, 2 in figure 4(*e*)). Colour bar is in radians. (*b*) Histogram of θ_n for the presented branch; $\theta/\pi = 0.182 \pm 0.05$, in $m = 5.5 \pm 1.5$, $n = 8.3 \pm 2.5$; (*c*) the mode structure for $t = 1140$ ms at 174.4 kHz; (*d*) the mode structure for $t = 1140$ ms at 183 kHz; $n/m = 9/6$ mode presents better agreement with experimental data. The mode is identified as $\mathrm{HAE}_{2,1}$.

9. MHD modelling for mode identification

Comparisons with computational MHD mode predictions indicate that some of the more prominent frequencies in the spectrogram can be identified with radially extended HAE (helical), GAE (global) and TAE (toroidal) Alfvén eigenmodes [1, 21]. The Alfvén mode structures are calculated using the AE3D code [22], while the continuum structures are obtained from the STELLGAP code [23].

The AE3D model solves a reduced set of shear Alfvén MHD eigenmode equations using the Jacobi–Davidson method that allows one to efficiently search for eigenmodes within finite range frequency windows centred around a target frequency. The mode structure includes the effects of couplings from the 3D equilibrium for both the continuum and eigenmode calculations. Nine toroidal modes were used to represent the eigenfunctions with the ranges of poloidal modes indicated in parentheses: $n = 1$ ($m = 0$–10), $n = 3$ ($m = 0$–10), $n = 5$ ($m = 0$–12), $n = 7$ ($m = 0$–12), $n = 9$ ($m = 0$–14), $n = 11$ ($m = 0$–18), $n = 13$ ($m = 0$–20), $n = 15$ ($m = 0$–25), $n = 17$ ($m = 0$–30).

The results of STELLGAP computations for the Alfvén continuum for the shot discussed earlier at $t = 1141$, #18838, are presented in figure 10 with the colours representing the dominant toroidal mode numbers, and the mode frequencies (241.1, 219.5, 183, 174.4, 159.4, 158.4 kHz) are obtained from AE3D modelling. Details of mode identification with frequency and spatial structure are given in figure 11 for a mode that is observed experimentally at 257 kHz at $t = 1141$ ms in shot #18838 (see also figure 4(*b*), where the discussed mode is marked by the upper yellow circle). In figure 11(*a*) the cross-phase θ_n between n_e oscillations observed in two poloidally shifted sample volumes is presented. Figure 11(*b*) shows the histogram of θ_n for the chosen branch, resulting in corrected $m = 4.4 \pm 2.2$. The radial structure of the mode with the frequency 241.1 kHz, displayed in figure 10, is shown in figure 11(*c*). Since this mode is dominated by the coupling between $n/m = 1/1$ and $n/m = 7/4$ components, it is classified as HAE. As explained in section 5, for this particular mode the experimental values are $m = 4.4 \pm 2.2$, so the estimated $n = 6.6 \pm 3.2$. The modelling results for $n/m = 7/4$ agree with the measured values within the existing experimental accuracy. These n/m values are in agreement with the low-order rational values that one would expect from the $\iota/2\pi$ profile (see figure 3). Finally, the experimentally observed $n/m = 7/4$ mode can be identified as a HAE.

The 3D structure of the identified mode is presented in figure 12. A minor difference in frequency (~6%) is expected due to effects of plasma flows and uncertainties in the plasma density, iota profile and average ion mass. A further example is given in figure 13 showing several modes with frequencies close to what is observed in the same shot at 177 and 181 kHz at $t = 1141$ ms (marked in figure 4(*b*) by the lower yellow circle). In figure 13(*a*) the θ_n spectrogram for this branch is presented. Figure 13(*b*) shows the histogram of θ_n for this branch, resulting in $m = 5.5 \pm 1.5$ and $n = 8.3 \pm 2.5$, according to the estimates in section 5.

The radial mode structure of the two closest modes with frequencies 174.4 kHz and 183 kHz (marked by the black horizontal lines in figure 10(*b*)) is presented in figures 13(*c*) and (*d*), respectively. Both modes are identified as $HAE_{2,1}$ since they both involve coupling of two dominant modes with differing m and n. The modelling results for $n/m = 9/6$ agree with the measured values within the existing experimental accuracy. These n/m values are in agreement with the low-order rational values that one would expect from the $\iota/2\pi$ profile (see figure 3). Minor differences in frequency (<1.5%) are expected due to effects of plasma flows and uncertainties in the plasma density and average ion mass.

For the cases examined here the density perturbations were also calculated along with the potential ones, presented in figures 11(*c*), 12 and 13(*c*) and (*d*). Calculation shows that the compressibility term (the second term in the density evolution equation (5)) is always larger than the first (density gradient) term by a factor that decreases with increasing frequency. For example, based on taking an rms average over the mode structure, the compressibility term is larger than the density gradient term by a factor of 102 for the 174.4 kHz mode, 45 for the 183 kHz mode and 14 for the 241 kHz mode.

10. Conclusions

The features and coherence characteristics of NBI-induced Alfvén eigenmodes were studied in the TJ-II heliac. The cross-phase between local oscillations of plasma potential and density was found to remain relatively constant for each individual AE branch. Poloidal rotation velocities and mode numbers were measured for the AEs, located in the core plasma for the first time with HIBP. It was shown that AE branches may rotate poloidally in both electron and ion drift directions. When the plasma density increases, the AE poloidal wavelength and mode number remain constant, while the poloidal rotation velocity decreases linearly with the AE frequency. The contribution of AEs to electrostatic bulk particle flux was studied, showing that there are significant peaks of the local flux correlated with different AE branches, which have different phase relations between E_{pol} and density oscillations. This would imply that they make different contributions to the flux: outward, inward and also zero. A comparison with computational MHD mode predictions indicates that some of the more prominent frequency branches can be identified as radially extended HAEs.

Acknowledgments

The authors are grateful to Professor Yu.N. Dnestrovskij and Professor K.A. Razumova for the continuous support of the activity of HIBP group and many valuable stimulating discussions. The authors are also grateful to Dr J. Ongena for the careful reading of the manuscript and many valuable comments. The work of the Russian team was supported by RFBR Grants 10-02-01385 and 11-02-00667.

References

[1] Jiménez-Gómez R. *et al* 2011 *Nucl. Fusion* **51** 033001
[2] Melnikov A.V. *et al* 2011 *Nucl. Fusion* **51** 083043
[3] Melnikov A.V. *et al* 2006 *Plasma Phys. Control. Fusion* **48** S87
[4] Fujisawa A. *et al* 2007 *Nucl. Fusion* **47** S718
[5] Melnikov A.V. *et al* 2010 *Nucl. Fusion* **50** 084023
[6] Ido T. *et al* 2010 *Plasma Phys. Control. Fusion* **52** 124025
[7] Estrada T. *et al* 2009 *Plasma Phys. Control. Fusion* **51** 124015
[8] Betti R. and Freidberg J. 1992 *Phys. Fluids* B **4** 1465
[9] Mishchenko A., Hatzky R. and Könies A. 2008 *Phys. Plasmas* **15** 112106
[10] Bondarenko I. *et al* 2001 *Rev. Sci. Instrum.* **72** 583
[11] Melnikov A.V. *et al* 2007 *Fusion Sci. Technol.* **51** 31 www.new.ans.org/pubs/journals/fst/a_1284
[12] Melnikov A.V. *et al* 2009 *Proc. 36th EPS Conf. on Plasma Physics (Sofia, Bulgaria, 2009)* P-4.186 http://epsppd.epfl.ch/Sofia/pdf/P4_186.pdf
[13] Melnikov A.V. *et al* 2011 *Plasma Fusion Res.* **6** 2402030 www.jspf.or.jp/PFR/PFR_articles/pfr2011S1/pfr2011_06-2402030.html
[14] Eliseev L.G. *et al* 2010 *Proc. 23rd Int. Conf. on Fusion Energy (Daejeon, Korea, 2010)* EXW/P7-17, http://www-pub.iaea.org/MTCD/meetings/cn180_papers.asp
[15] Eliseev L.G. *et al* 2012 *Plasma Fusion Res.* **7** 2402064 www.jspf.or.jp/PFR/PFR_articles/pfr2012S1/pfr2012_07-2402064.html
[16] Melnikov A.V. *et al* 2010 *Proc. 37th EPS Conf. on Plasma Physics (Dublin, Ireland, 2010)* P1.066 http://ocs.ciemat.es/EPS2010PAP/pdf/P1.066.pdf
[17] Nazikian R. *et al* 2003 *Phys. Rev. Lett.* **91** 125003
[18] Sharapov S. *et al* 2004 *Phys. Rev. Lett.* **93** 165001
[19] Smolyakov A., Callen J. and Hirose A 1993 *Proc. Int. School of Plasma Physics 'Piero Caldirola' (Varenna, Italy, 1993)* vol 14, p 87 http://en.sif.it/books/series/proceedings_plasma
[20] Isichenko M., Gruzinov A. and Diamond P. 1995 *Phys. Rev. Lett.* **74** 4436
[21] Melnikov A.V. *et al* 2010 *Plasma Fusion Res.* **5** S2019
[22] Spong D.A., D'Azevedo E. and Todo Y. 2010 *Phys. Plasmas* **17** 022106
[23] Spong D.A., Sanchez R. and Weller A. 2003 *Phys. Plasmas* **10** 3217